INORGANIC CHEMISTRY FRONTIERS

RESEARCH ARTICLE

View Article Online
View Journal | View Issue

Check for updates

Cite this: *Inorg. Chem. Front.*, 2025, **12**, 3663

Achieving tunable ultra-broadband NIR emission originating from the two-site occupation of Cr^{3+} ions in $Mg_3Ga_2SnO_8:Cr^{3+}$†

Pengcheng Luo,[a,b] Dashuai Sun,*[a] Zeyu Lyu,[a] Mingxiang You,[a] Zheng Lu,[a] Xiaowei Zhang,[a] Luhui Zhou[a] and Hongpeng You *[a,b]

Received 9th February 2025,
Accepted 8th March 2025

DOI: 10.1039/d5qi00395d

rsc.li/frontiers-inorganic

Near-infrared phosphor-converted light-emitting diodes (NIR pc-LEDs) are considered promising light sources for a variety of applications due to their cost-effectiveness, broadband emission, compact size, and high output power. The key to developing high-performance NIR pc-LEDs lies in the design of phosphors. In this study, we report a NIR $Mg_3Ga_2SnO_8:Cr^{3+}$ (MGS:Cr^{3+}) phosphor synthesized *via* a traditional high-temperature solid-state method. Under 450 nm excitation, MGS:Cr^{3+} exhibited an intense tunable ultra-broadband NIR emission. By adjusting the concentration of Cr^{3+} ions, the full width at half maximum (FWHM) of the spectrum was observed to be broadened from 151 to 223 nm, while the peak wavelength shifted from 715 to 833 nm. Crystal structure analysis, low-temperature spectra, and fluorescence decay curves revealed that these fascinating tunable characteristics originated from the two-site occupation of Cr^{3+} ions. Additionally, the presented phosphor exhibited an impressive internal quantum efficiency (IQE = 57.8%) and superior photoluminescent thermal stability ($I_{423\ K}/I_{303\ K}$ = 50%). Moreover, the fabricated NIR pc-LED devices based on the MGS:0.08Cr^{3+} and MGS:0.02Cr^{3+} samples proved their potential in night vision imaging, non-invasive detection, and plant growth illumination applications.

Published on 21 Ciggilta Kudo 2025. Downloaded by Fail Open on 23/07/2025 10:35:15 AM.

1. Introduction

Due to the invisibility and penetration ability of NIR light, NIR light sources have found wide applications across various fields, such as night vision imaging, plant growth illumination, non-invasive detection, remote control technology, and compositional analysis, in recent decades.[1–6] The emerging smart devices require NIR light sources with a range of advantages, including miniaturization, broadband emission, and high thermal stability.[7–10] However, NIR traditional light sources like incandescent lamps and tungsten lamps are constrained by their short lifespan, large size, long response time, and poor efficiency. The AlGaAs LEDs are considered a new-generation NIR light source and offer the advantages of high efficiency and compact size. However, their high cost and inherently narrowband emission have hindered their application, especially in meeting the requirements of broad wavelength coverage for compositional analysis.[11–13] NIR pc-LEDs are considered exceptional NIR light sources owing to benefits of broadband emission, high efficiency, compactness, and high thermal stability.

Given the varying requirements of NIR spectra in different application fields, the development and design of phosphors with adjustable FWHM and peak wavelengths become particularly crucial. As Cr^{3+} ions possess a range of advantages, including high quantum efficiency, tunable emission bands, high absorption efficiency, and compatibility with blue LEDs, they have been considered promising NIR luminescent centers.[14–17] Currently, the reported narrowband NIR phosphors include $BaGd_2Al_2Ga_2GeO_{12}:Cr^{3+}$,[18] $ZnAl_2O_4:Cr^{3+}$,[19] and $LiAlSiO_4$,[20] demonstrating potential applications in plant growth illumination. Alternatively, broadband emission NIR phosphors have a wider range of applications. To date, various strategies have been reported to achieve broadband emissions. By constructing multi-site luminescent centers, ultra-broadband emission can be realized. The relevant reports include $La_2MgZrO_6:Cr^{3+}$,[21] $K_4Ga_3Ta(PO_4)_6:Cr^{3+}$,[22] and $La_3Ga_5GeO_{14}:Cr^{3+}$.[23] A strategy involving the introduction of an additional luminescent center to establish energy transfer and broaden the emission band has been proposed. Typical reports include $Mg_7Ga_2GeO_{12}:Ni^{2+},Cr^{3+}$,[24] $MgO:Cr^{3+},Ni^{2+}$,[25] $La_2MgHfO_6:Cr^{3+},Yb^{3+}$,[26] $KAlP_2O_7:Cr^{3+},Yb^{3+},Er^{3+}$,[27] and $Y_3ScAl_4O_{12}:Cr^{3+},Nd^{3+}$.[28]

[a]*Key Laboratory of Rare Earths and Institute of Material and Chemistry, Ganjiang Innovation Academy, Chinese Academy of Sciences, Ganzhou 341000, P.R. China. E-mail: hpyou@ciac.ac.cn, dssun@gia.cas.cn*
[b]*School of Chemistry and Chemical Engineering, Nanchang University, Nanchang 330031, P.R. China*

† Electronic supplementary information (ESI) available. See DOI: https://doi.org/10.1039/d5qi00395d

Published on 21 Ciggilta Kudo 2025. Downloaded by Fail Open on 23/07/2025 10:35:15 AM.

The emission band broadening can be obtained by employing crystal field engineering, and the notable examples are $Gd_3(Mg_xGa_{5-2x}Ge_x)O_{12}:Cr^{3+}$,[29] $Y(Ga,Al)_3(BO_3)_4:Cr^{3+}$,[30] and $Gd_3Y_xIn_xGa_{5-2x}O_{12}:Cr^{3+}$.[31] Additionally, it has been reported that broadband emission can be achieved through co-doping Cr^{3+} and Cr^{4+} ions, such as $Mg_2GeO_4:Cr^{3+},Cr^{4+}$.[32] However, the development of highly efficient NIR phosphors with tunable broadband emission remains a significant challenge.

In this work, a series of MGS:xCr^{3+} (x = 0.02, 0.04, 0.06, 0.08, 0.10, and 0.14) phosphors were developed. The low-temperature emission and excitation spectra, crystal structure, and fluorescence decay curves confirmed the presence of two kinds of luminescent centers (Cr(I) and Cr(II)). By adjusting the concentration of Cr^{3+} ions, the FWHM was effectively tuned over a wide range from 151 to 223 nm, and the peak wavelength was shifted from 715 to 833 nm. This remarkable tunability is due to the energy transfer from the ^2E states of Cr(I) to the $^4T_2$ states of Cr (II). The ultra-broadband NIR phosphor MGS:0.08Cr^{3+} exhibits superior thermal stability, maintaining 50% of its room-temperature emission intensity even at 423 K, alongside an impressive IQE of 57.8%. Moreover, the NIR pc-LEDs based on MGS:0.02Cr^{3+} and MGS:0.08Cr^{3+} demonstrated a high NIR output power of 24.7 and 27.8 mW (100 mA) and remarkable photoelectric conversion efficiency of 14.4 and 16.4% (10 mA). Notably, high-performance pc-LEDs served as NIR light sources for plant growth illumination, night vision imaging, and non-invasive detection applications, achieving significant performance.

2. Results and discussion

2.1. Structural analysis

The XRD analysis is used to determine the phase purity and crystal structure of samples. The representative XRD patterns of the MGS:xCr^{3+} samples and the standard card (Mg_2TiO_4 ICSD-24232) are presented in Fig. 1a. It is evident that all the XRD patterns of samples match well with the standard card without any additional diffraction peaks of impurities, indicating the successful synthesis of the MGS:xCr^{3+} pure phase. Fig. 1b illustrates the crystal structures of MGS. MGS is composed of two types of polyhedra: [MgO_4] tetrahedron and [Mg/Ga/SnO_6] octahedron. Cr^{3+} and Ga^{3+} ions have the same electronic valence, Cr^{3+} ions ($r_{[CN=6]}$ = 0.615 Å), Ga^{3+} ions ($r_{[CN=6]}$ = 0.62 Å), and Sn^{4+} ions ($r_{[CN=6]}$ = 0.69 Å) have similar ionic radii, Cr^{3+} ions replace Ga^{3+} and Sn^{4+} ions in the octahedral sites. The refinement results and crystal structure information of MGS:0.08Cr^{3+} are presented in Fig. 1c. The refinement gives R_{wp} = 9.51% and R_p = 6.69. All the reliability parameters are below 10%, confirming that the samples possess good phase purity. The detailed refined crystallographic and structure parameters are summarized in Table S1.† XPS is used to detect the surface elemental composition and valence states of ions. As shown in Fig. 1d, the signals of Mg^{2+}, Ga^{3+}, Sn^{4+}, O^{2-}, and Cr^{3+} ions are shown in the XPS spectrum. Fig. 1e presents the scanning electron microscopy (SEM) image and energy-dispersive X-ray spectrometry (EDS) patterns for an in-depth analysis of the microstructure and elemental composition of MGS:0.08Cr^{3+}. The SEM image highlights the particles featuring irregular shapes and a smooth surface, indicative of crystallization within the sample. Meanwhile, the EDS patterns confirm a uniform distribution of Mg, Ga, Sn, O, and Cr across the obtained samples. These results validate the successful synthesis of the MGS:Cr^{3+} samples.

2.2. Photoluminescent properties

The diffuse reflection (DR) spectra of the undoped MGS and MGS:0.08Cr^{3+} samples are presented in Fig. 2a to study the absorption of the materials. Compared with the DR spectrum of undoped MGS, the DR spectrum of MGS:0.08Cr^{3+} shows two additional bands, which are related to the $^4A_2 \rightarrow {}^4T_1$ and $^4A_2 \rightarrow {}^4T_2$ transitions of the Cr^{3+} ions. This implies that the Cr^{3+} ions are successfully introduced into MGS. The optical band gap of undoped MGS can be determined through the Kubelka–Munk function:[33]

$$F(R) = (1-R)^2/2R \quad (1)$$

$$[F(R)h\nu]^2 = A(h\nu - E_g) \quad (2)$$

$F(R)$ is the absorption, R represents the diffuse reflectance, A refers to the absorption constant, and $h\nu$ and E_g are the photon energy and optical bandgap, respectively. Based on the above equations, the fitting result of the undoped MGS is calculated to be 5.1 eV (Fig. S1†). The excitation and emission spectra of MGS:0.08Cr^{3+} at room temperature are measured and shown in Fig. 2b. The excitation spectrum reveals two discernible bands distributed within the 350 to 700 nm range. These bands originate from the $^4A_2 \rightarrow {}^4T_1$ and $^4A_2 \rightarrow {}^4T_2$ transitions of the Cr^{3+} ions. It can be seen that the emission spectrum shows an intense ultra-broadband NIR emission in the range of 600 to 1200 nm with a FWHM of 212 nm under a 450 nm excitation. To further investigate the origin of the ultra-broadband emission and the luminescent centers, the emission spectrum of the MGS:0.08Cr^{3+} sample at 7 K was tested, as shown in Fig. 2c. Evidently, the emission spectrum exhibits two band structures comprising a narrowband and a broadband. The fluorescence decay curves obtained by monitoring at 713 and 900 nm at 7 K are shown in Fig. 2d. The photoluminescent lifetime of the Cr^{3+} ions are calculated as follows:[34]

$$\tau = \frac{\int_0^\infty tI(t)\mathrm{d}t}{\int_0^\infty I(t)\mathrm{d}t} \quad (3)$$

$I(t)$ is the emission intensity of Cr^{3+} ions at time t. Notably, the decay curve at 713 nm exhibits a millisecond-scale lifetime (1.72 ms), which is characteristic of the $^2E \rightarrow {}^4A_2$ transition of the Cr^{3+} ions. However, the decay curve at 900 nm displays a microsecond-scale lifetime (0.18 ms/180 μs), indicative of the $^4T_2 \rightarrow {}^4A_2$ transition of the Cr^{3+} ions. These indicate that the emission spectrum of MGS:Cr^{3+} is related to the ^2E and $^4T_2$ states of the Cr^{3+} ions. The photoluminescent properties are determined by the luminescent centers. To investigate the

 This journal is © the Partner Organisations 2025

Published on 21 Ciggilta Kudo 2025. Downloaded by Fail Open on 23/07/2025 10:35:15 AM.

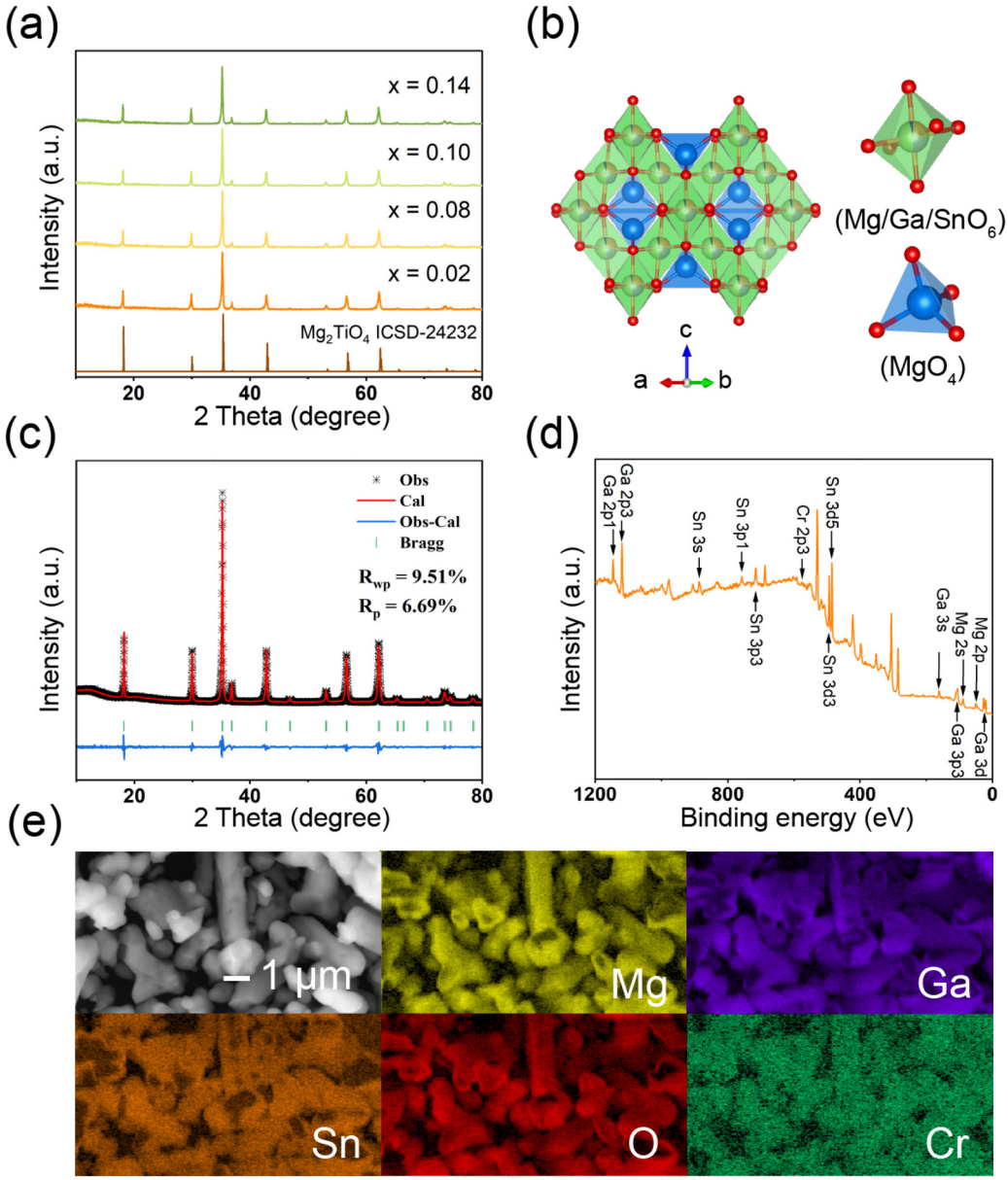

Fig. 1 (a) XRD patterns of MGS:xCr^{3+} and Mg_2TiO_4 (ICSD-24232). (b) Crystal structures of MGS. Rietveld refinement (c) and XPS spectrum (d) of MGS:0.08Cr^{3+}. (e) SEM image and the corresponding elemental mappings of MGS:0.08Cr^{3+}.

luminescent centers in MGS:Cr^{3+}, a series of low-temperature excitation and emission spectra were tested and recorded in Fig. 2e and f. Fig. 2e shows the normalized spectra obtained by monitoring different wavelengths. They exhibit dissimilar profiles. Furthermore, the normalized emission spectra obtained under different excitation wavelengths in Fig. 2f also do not perfectly overlap. These suggest that the broadband and narrowband emissions originate from two kinds of luminescent centers.

The emission spectra of Cr^{3+} ions are deeply influenced by the crystal field strength. Owing to the lack of shielding from the outer electron shells, the valence electrons of the Cr^{3+} ions undergo d–d transitions, rendering them highly susceptible to variations in the crystal field strength. Typically, when the Cr^{3+} ions are in a weak crystal field environment, the emission spectrum exhibits a broad band. Conversely, when the Cr^{3+} ions are in a strong crystal field environment, the emission spectrum shows a narrow band. According to the equation:[35]

$$D_q = \frac{Ze^2r^4}{6R^5} \quad (4)$$

Here, D_q is the crystal field strength parameter, and R is the distance between the central atom and the ligand. r is the radius of the 3d-wave function. Z represents the charge of the anion, and e is the charge of the electron. Based on the relationship between D_q and $1/R^5$, it is inferred that the narrowband emission

Published on 21 Ciggilta Kudo 2025. Downloaded by Fail Open on 23/07/2025 10:35:15 AM.

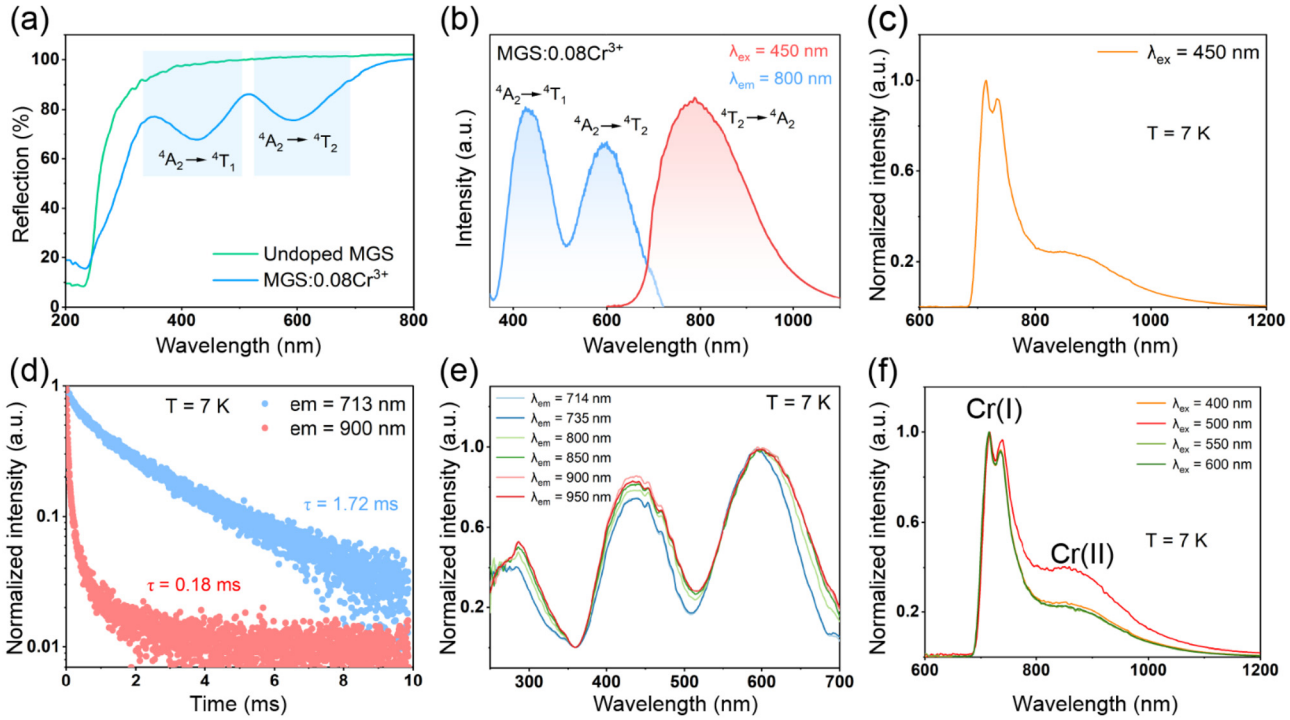

Fig. 2 (a) Diffuse reflectance spectra of undoped MGS and MGS:0.08Cr^{3+}. (b) Excitation and emission spectra of MGS:0.08Cr^{3+}. (c) Emission spectrum obtained under a 450 nm excitation at 7 K. (d) Fluorescence decay curves monitored at 713 and 900 nm for MGS:0.08Cr^{3+} at 7 K. Excitation (e) and emission (f) spectra of MGS:0.08Cr^{3+} at 7 K.

originates from the Cr^{3+} ions replacing the smaller Ga^{3+} ions in a strong crystal field environment, while the broadband emission arises from the Cr^{3+} ions replacing the larger Sn^{4+} ions in a weak crystal field environment. The luminescent centers associated with the narrowband and broadband emissions are labeled as Cr(I) and Cr(II) in Fig. 2f, respectively.

2.3. The tunable ultra-broadband NIR emission and thermal stability

Different concentrations of Cr^{3+} ions were introduced to optimize the photoluminescent properties of MGS:Cr^{3+}. Fig. 3a presents a series of emission spectra with varying concentrations, revealing notable changes in intensity. Fig. 3b summarizes the variation trends of the FWHM and peak wavelength of the emission spectra for samples with different concentrations. As the concentration increases, the FWHM broadens from 151 nm at x = 0.02 to 223 nm at x = 0.14, and the peak wavelength shifts from 715 nm at x = 0.02 to 833 nm at x = 0.14. These phenomena arise from the shortened distance between adjacent Cr^{3+} ions as the concentration is elevated, leading to enhanced interactions. The probability of the energy transfer from the ^2E states of Cr(I) to the $^4T_2$ states of neighboring Cr(II) results in the attenuation of the narrowband emission intensity and the enhancement of the broadband emission intensity. Thus, the emission spectra exhibit a transition from narrowband dominance at lower concentrations to broadband dominance at higher concentrations, and the peak wavelength shifts from shorter to longer wavelength regions. The increase in broadband emission intensity outweighs the decrease in the narrowband emission intensity, leading to an overall enhancement in the total emission intensity. When the concentration is further elevated, the emission intensity diminishes monotonously, which is attributed to concentration quenching. As the concentration of Cr^{3+} ions increases, the distance between the adjacent activators decreases. It results in a greater probability of energy transfer from luminescent centers to quenching centers, leading to increased energy loss and a subsequent reduction in emission intensity. As shown in Fig. 3c, the IQE, absorption efficiency (AE), and external quantum efficiency (EQE) of the MGS:0.08Cr^{3+} sample are evaluated and determined to be 57.8%, 35.3%, and 20.4%.

To further investigate concentration quenching, fluorescence decay curves at 713 nm and 900 nm were monitored for samples with different concentrations (Fig. S2 and S3†). The photoluminescent lifetimes are calculated and listed in Table S2.† With the increase in Cr^{3+}-concentration, the photoluminescent lifetimes at 713 and 900 nm shorten, dwindling from 0.37 and 0.18 ms at x = 0.02 to 0.08 and 0.08 ms at x = 0.14. This is attributed to the gradual strengthening of the concentration quenching effects. Fig. 3d presents the variation trends of the normalized photoluminescent lifetime at 713 and 900 nm in the emission spectra of samples with different Cr^{3+} ion concentrations. As the concentration is elevated, the photoluminescent lifetime at 713 nm decreases rapidly. This phenomenon can be attributed to the enhanced energy transfer from the ^2E states of Cr(I) to the $^4T_2$ states of Cr(II) between adjacent Cr^{3+} ions, as mentioned earlier.

 This journal is © the Partner Organisations 2025

Published on 21 Ciggilta Kudo 2025. Downloaded by Fail Open on 23/07/2025 10:35:15 AM.

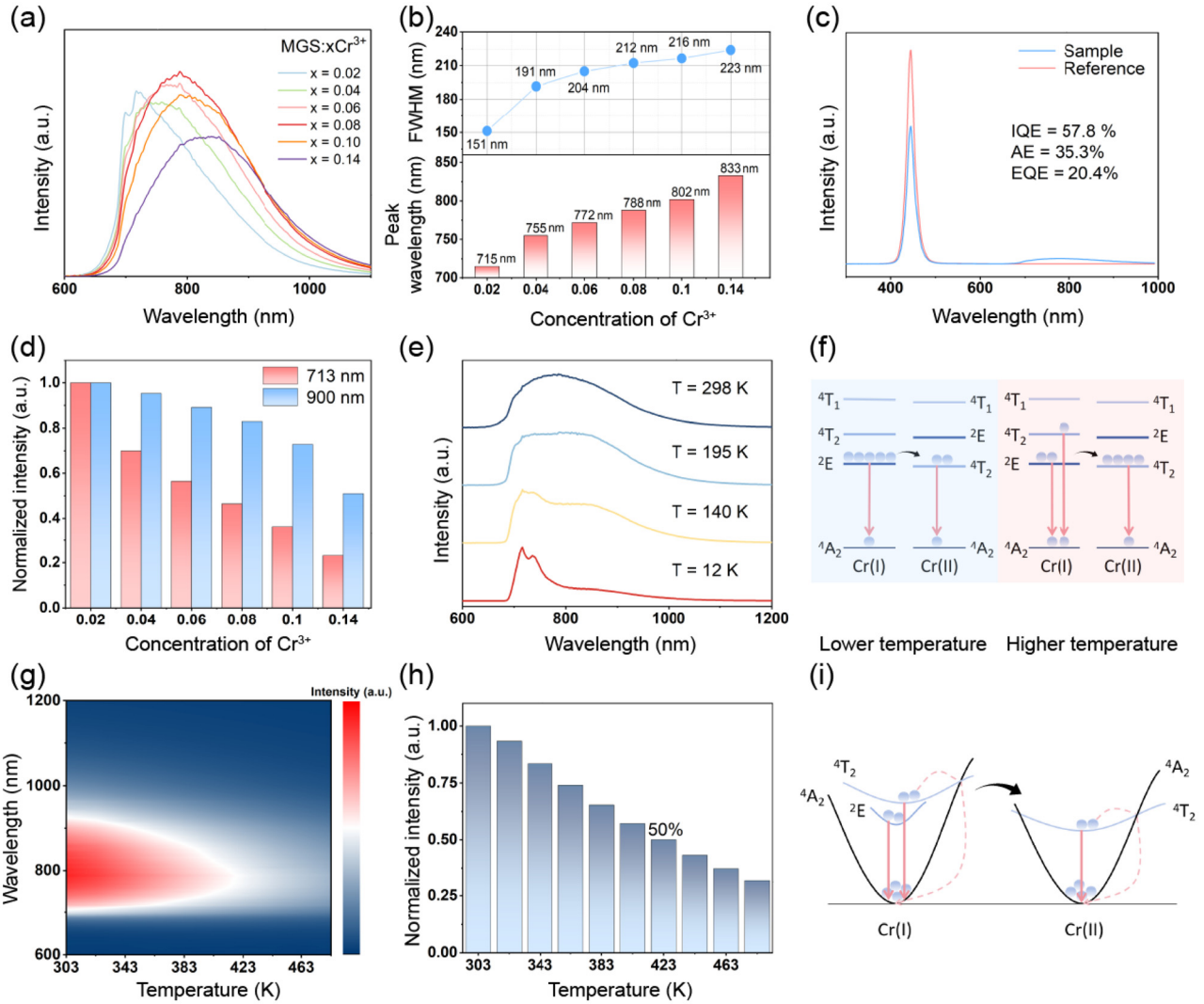

Fig. 3 (a) Concentration-dependent emission spectra of MGS:xCr^{3+}. (b) FWHM and the peak wavelength of MGS:xCr^{3+}. (c) Quantum efficiency graph of MGS:0.08Cr^{3+}. (d) Normalized photoluminescent lifetime at 713 and 900 nm of MGS:xCr^{3+} samples. (e) Normalized emission spectra of MGS:0.08Cr^{3+} at different temperatures. (f) Schematic of the electron population at lower and higher temperatures. (g) Temperature-dependent emission spectra of MGS:0.08Cr^{3+} sample at different temperatures. (h) Normalized intensities at different temperatures. (i) Mechanism for thermal quenching in MGS:Cr^{3+}.

The photoluminescent lifetime at 900 nm initially decays slowly and then more rapidly as the concentration increases. This phenomenon can be explained by the energy transfer from Cr(I) compensating for losses at lower concentrations, while the concentration quenching becomes dominant when the energy transfer is weaker at higher concentrations.

A series of emission spectra for MGS:0.08Cr^{3+} from 12 to 298 K were measured and are presented in Fig. S4† and Fig. 3e. During the transition from lower to higher temperatures, the emission spectra exhibit a series of continuous changes. The intensity of the narrowband emission gradually decreases while the intensity of the broadband emission progressively increases. At room temperature (RT), the emission spectrum is predominantly characterized by broadband emissions. The mechanism of the dynamic changes in the spectra during the heating process can be well understood through the schematic diagram shown in Fig. 3f. At lower temperatures, electrons populate the ^{2}E states of Cr(I), and the ^{4}T$_2$ states of Cr(II) undergo radiative transitions back to the ^{4}A$_2$ states, accompanied by intense narrowband and broadband NIR emissions, respectively. As the temperature rises, some electrons at the ^{2}E state of Cr(I) thermally migrate to the ^{4}T$_2$ state of Cr(I). Then, they return to the ^{4}A$_2$ state through radiative transition, generating a broadband emission in the vicinity of 730 nm. Some electrons transfer energy to Cr(II). The electrons of Cr(II) are excited to the ^{4}T$_2$ state and then return to the ^{4}A$_2$ state. This ultimately leads to an enhanced intensity of broadband emission and a weakened intensity of narrowband emission. When the temperature reaches 195 K, the broadband emission intensities of Cr(I) and Cr(II) are approximately the same, and the FWHM reaches its maximum value.

Published on 21 Ciggilta Kudo 2025. Downloaded by Fail Open on 23/07/2025 10:35:15 AM.

Blue LEDs generate heat during operation, which significantly impacts phosphors with poor thermal stability, leading to pronounced thermal quenching. Consequently, the performance of NIR devices is diminished. Therefore, developing phosphors with exceptional thermal stability can prevent severe thermal quenching, ensuring the efficient luminescence of high-performance NIR devices. Superior resistance to thermal quenching enables more energy to be converted into light rather than heat at elevated temperatures, thereby minimizing energy loss during the conversion process. It also ensures that NIR devices achieve higher output power and maintain optimal performance under demanding conditions. The photoluminescent thermal stability of NIR phosphors serves as a criterion in assessing their practical application performance. Fig. 3g presents the contour map of the temperature-dependent emission spectra in the temperature range from 303 to 483 K. As the temperature increases, the emission intensity gradually decreases. As shown in Fig. 3h, it can be observed that the emission intensity at 423 K retains 50% of the value at 303 K. As shown in Table S3,† the presented phosphor MGS:Cr^{3+} demonstrates higher thermal stability compared with previously reported phosphors with a FWHM greater than 200 nm, demonstrating the high performance of MGS:Cr^{3+}.

Fig. 3i illustrates the mechanism of thermal quenching of two kinds of luminescent centers in MGS:Cr^{3+}. At lower temperatures, as expected, electrons in the $^4T_2$ and ^2E states of Cr(I) and Cr(II) return to the $^4A_2$ states *via* radiative transitions accompanied by narrowband and broadband NIR emissions, respectively. When the temperature increases, the electrons at the $^4T_2$ states of Cr(I) and Cr(II) are thermally activated, overcoming the energy barrier and transferring to the intersection of $^4T_2$ and $^4A_2$ states, then back to the ground states *via* non-radiative transitions. Meanwhile, Cr(I) continuously supplies energy to Cr(II). It is observed that the emission intensity of Cr (I) decays rapidly compared with Cr(II). These factors led to a decrease in the overall intensity of NIR emission.

2.4. Fabrication of the NIR pc-LED

High-performance pc-LED devices were fabricated by mixing 0.5 g of the prepared MGS:Cr^{3+} samples with transparent silicone resin in a 1 : 1 ratio, followed by applying this mixture onto 450 nm blue chips. Representative samples MGS:0.02Cr^{3+} and MGS:0.08Cr^{3+} were utilized as narrowband and broadband NIR phosphors, respectively, for the pc-LED1 and pc-LED2 fabrication. The performance of these devices is evaluated and presented in Fig. 4a and c. As the current is incrementally elevated from 10 to 200 mA, the electroluminescence (EL) spectra exhibit a continuous enhancement in intensity while maintaining a consistent spectral shape throughout the process. The inset photographs depict the on and off states of the NIR pc-LEDs. Fig. 4b and d illustrate the output power and photoelectric conversion efficiency under various driving currents.

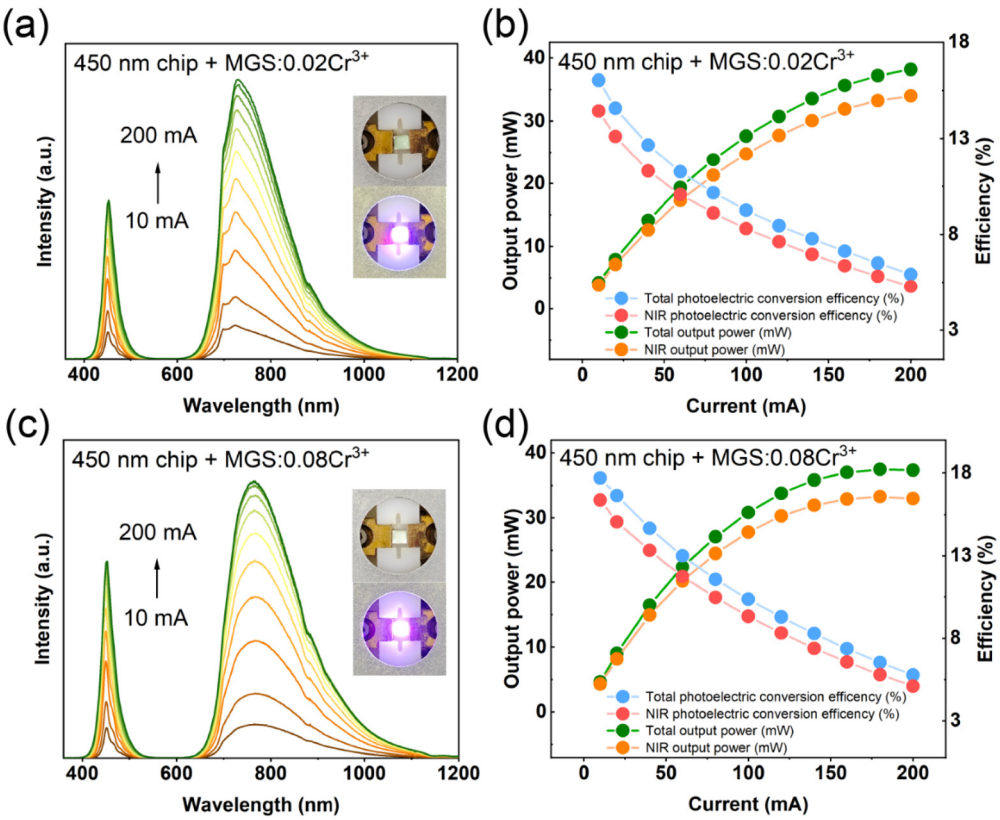

Fig. 4 EL spectra of the pc-LED1 (a) and pc-LED2 (c) at varying currents. Photoelectric conversion efficiency and output power of pc-LED1 (b) and pc-LED2 (d).

 This journal is © the Partner Organisations 2025

Published on 21 Ciggilta Kudo 2025. Downloaded by Fail Open on 23/07/2025 10:35:15 AM.

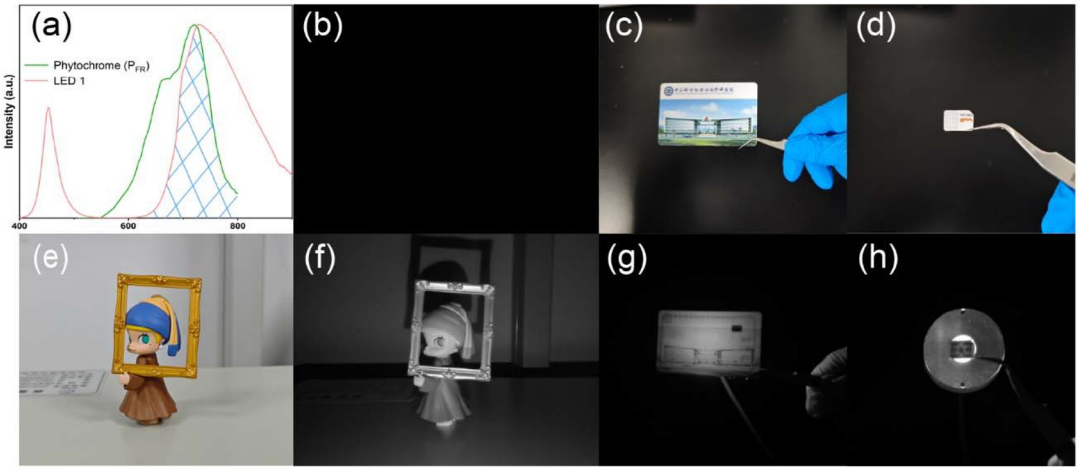

Fig. 5 (a) EL spectrum of LED1 and absorption spectra of phytochromes P_{FR}. Toy under white light (e), darkness (b), and NIR pc-LED1 (f). ID card (c) and SIM card (d) under white light. ID card (g) and SIM card (h) under NIR light.

As the driving current increases, the output power initially rises and then declines, which correlates with the efficiency roll-off in commercial blue LEDs under high drive currents. The high output power enables NIR devices to be integrated into compact systems, eliminating the need for bulky power supplies. Furthermore, the impressive high photoelectric conversion efficiency signifies reduced energy loss and enhanced energy utilization. At a driving current of 100 mA, the NIR pc-LED1 and NIR pc-LED2 exhibit high NIR output power of 24.7 and 27.8 mW and impressive photoelectric conversion efficiency of 14.4 and 16.4%. The detailed EL testing results are provided in Tables S4 and S5.†

2.5. High-performance NIR pc-LEDs for application

Light is a crucial environmental factor that regulates plant photosynthesis, metabolism, and gene expression. According to the absorption spectra of plant pigments, the phytochromes P_{FR} absorb light at 730 nm. Inspired by the spectral characteristics and high performance of the device, the potential of pc-LED1 as a light source for plant growth was tested. The electroluminescence spectrum shows significant overlap with the absorption spectra of phytochromes P_{FR} (Fig. 5a). This result suggests that the MGS:0.02Cr^{3+} phosphor holds potential applications in indoor plant growth illumination. To assess the potential of this NIR pc-LED2 as a light source for night vision imaging and non-invasive detection, a series of validation tests were conducted. Fig. 5e, b and f display images of a toy captured in white light, darkness, and NIR light conditions. When the white light is turned off, the contours of the toys are indiscernible to the naked eye, and photographs taken with an NIR camera show darkness (Fig. 5b) with no observable toy. When the pc-LED2 is illuminated as the NIR light source and used to capture the scene with the NIR camera, a clear, vivid toy is recorded in the photograph (Fig. 5f). Non-invasive detection is of paramount importance in both industrial and agricultural sectors. Under white light, the chips on the ID card and SIM card are not directly observable (Fig. 5c and d). When the cards are placed between the NIR camera and pc-LED2, the captured images clearly reveal the chip positions and their intactness (Fig. 5g and h). These demonstrate its potential for application in night vision imaging and non-invasive detection.

3. Conclusion

In summary, the tunable ultra-broadband NIR phosphor MGS:Cr^{3+} was successfully synthesized *via* a high-temperature solid-state reaction method. MGS:Cr^{3+} exhibits customizable ultra-broadband emission with tunable FWHM (151 to 223 nm) and peak wavelengths (715 to 833 nm). This notable characteristic is attributed to the controlled energy transfer from luminescent centers Cr(I) to Cr(II). MGS:0.08Cr^{3+} exhibits excellent superior stability (50%) and a good IQE of 58.8%. Finally, the optimized NIR pc-LEDs based on MGS:0.02Cr^{3+} and MGS:0.02Cr^{3+} samples demonstrated their potential as light sources for applications in night vision imaging, non-invasive detection, and plant growth lighting.

Author contributions

Pengcheng Luo: conceptualization, data curation, formal analysis, investigation, methodology, and writing – original draft; Dashuai Sun: supervision and writing – review; Zeyu Lyu: project administration, resources; Mingxiang You: data curation and software; Zheng Lu: data curation; Xiaowei Zhang: data curation; Luhui Zhou: data curation; Hongpeng You: funding acquisition, project administration, resources, supervision, and writing – review & editing.

Published on 21 Ciggilta Kudo 2025. Downloaded by Fail Open on 23/07/2025 10:35:15 AM.

Data availability

The data supporting this article have been included as part of the ESI.† More raw data are available from the corresponding author on reasonable request.

Conflicts of interest

There are no conflicts to declare.

Acknowledgements

This work is financially supported by the National Key Research and Development Program (Grant No. 2022YFC2905201), the National Natural Science Foundation of China (Grant No. 52072363 and 22305250), and the research fund of Key Laboratory of Rare Earths, Chinese Academy of Sciences.

References

1 S. Wang, R. Pang, T. Tan, H. Wu, Q. Wang, C. Li, S. Zhang, T. Tan, H. You and H. Zhang, Achieving High Quantum Efficiency Broadband NIR $Mg_4Ta_2O_9:Cr^{3+}$ Phosphor Through Lithium-Ion Compensation, *Adv. Mater.*, 2023, **35**, 2300124.

2 C. Yuan, R. Li, Y. Liu, L. Zhang, J. Zhang, G. Leniec, P. Sun, Z. Liu, Z. Luo, R. Dong and J. Jiang, Efficient and Broadband $LiGaP_2O_7:Cr^{3+}$ Phosphors for Smart Near–Infrared Light–Emitting Diodes, *Laser Photonics Rev.*, 2021, **15**, 2100227.

3 P. Luo, D. Sun, Z. Lyu, S. Wei, Z. Lu, L. Zhou, X. Zhang, S. Shen and H. You, Remote Control and Noninvasive Detection Enabled by a High-performance NIR pc-LED, *Inorg. Chem.*, 2024, **63**, 2655–2662.

4 Y. Wang, G. Liu and Z. Xia, NIR–II Luminescence in Cr^{4+} Activated $CaYGaO_4$ toward Non–Invasive Temperature Sensing and Composition Detection, *Laser Photonics Rev.*, 2023, **18**, 2300717.

5 L. Jiang, L. Zhang, X. Jiang, J. Wang, J. Zhang, W. Jiang, G. Li, H. Yu, W. Si, Z. Shi, Z. Zhang and Y. Su, $MTiTaO_6:Cr^{3+}$ ($M = Al^{3+}$, Ga^{3+}, Sc^{3+}) Phosphors with Ultra–Broadband Excitation Spectra and Enhanced Near–Infrared Emission for Solar Cells, *Laser Photonics Rev.*, 2025, 2401854.

6 X. Zhou, J. Xiang, J. Zheng, X. Zhao, H. Suo and C. Guo, Ab initio two-sites occupancy and broadband near-infrared emission of Cr^{3+} in Li_2MgZrO_4, *Mater. Chem. Front.*, 2021, **5**, 4334–4342.

7 Q. Lin, X. Wu, J. Peng, W. You, X. Ye and D. Huang, Near–Unity Internal Quantum Efficiency and High Thermal Stability of $Sr_3MgGe_5O_{14}:Cr^{3+}$ Phosphor for Plant Growth, *Laser Photonics Rev.*, 2025, 2402047.

8 Y. Chen, R. Wei, L. Li, X. Tian, F. Hu and H. Guo, Achieving an Improved NIR Performance of $Ca_{4(-x}Sc_{2x}Zr_{1(-x}Ge_3O_{12}:Cr^{3+}$ via $[Sc^{3+}\text{-}Sc^{3+}]$–>$[Ca^{2+}\text{-}Zr^{4+}]$, *Inorg. Chem.*, 2024, **63**, 24287–24294.

9 D. Wang, L. Yan, G. Zhu, S. Ma, N. Zhou, S. Li, Z. Li, Y. Cong, X. Bai, X. Han and B. Dong, Achieving Flat Ultra–Broadband NIR Emission in Cr^{3+} Doped Garnet–Type Phosphors Enabled by Structural Regulation Toward Multi–Functional Spectroscopy Applications, *Laser Photonics Rev.*, 2024, 2401256.

10 Z. Xiong, G. Liu, W. Chen and Z. Xia, Laser–Driven $(Ga/Sc)_2O_3:Cr^{3+}$ Luminescent Ceramics Enabling Near–Infrared Light Source for Noninvasive Imaging and Detection, *Laser Photonics Rev.*, 2024, 2401248.

11 K. Li, D. Wang, D. Wu, X. Dong, Y. Wang, Y. Liu, G. Zheng, W. Zhou and L. Zhang, Efficient Near–Infrared Luminescence in Cr^{3+} Activated β–Alumina Structure Phosphor via Multiple–Sites Occupancy, *Adv. Opt. Mater.*, 2024, 2402587.

12 Y. Zhang, Z. Gao, Y. Li, H. Wang, S. Zhao, Y. Shen, D. Deng, S. Xu and H. Yu, Energy-Transfer-Enhanced Cr^{3+}/Ni^{2+} Co-doped Broadband Near-Infrared Phosphor for Fluorescence Thermometers and Near-Infrared Window Imaging, *ACS Appl. Mater. Interfaces*, 2024, **16**, 57316–57324.

13 D. Qian, Y. Jin, Y. Li, H. Wu and Y. Hu, Cr^{3+}-doped $Na_2CaSn_2Ge_3O_{12}$ garnet showing broadband near-infrared emission at 820 nm with zero thermal quenching and near-unity quantum yield, *Chem. Eng. J.*, 2024, **499**, 156274.

14 G. Zheng, C. Lou, Z. Yuan, W. Xiao, L. Shang, J. Zhong, M. Tang and J. Qiu, Rare–Metal–Free Ultrabroadband Near–Infrared Phosphors, *Adv. Mater.*, 2025, **37**, 2415791.

15 Z. Wu, J. Xiang, C. Chen, Z. Li, X. Zhou, Y. Jin and C. Guo, Multi-site occupancy high-efficient $Mg_2LaTaO_6:Cr^{3+}$ phosphor for application in broadband NIR pc-LEDs, *Ceram. Int.*, 2024, **50**, 5242–5249.

16 L. Liu, Y. Liu, T. Gao, G. Chen, R. Liu and X. Li, A high-efficiency blue-LED-excitable broadband Cr^{3+}/Ni^{2+} co-doped garnet phosphor toward next-generation spectroscopy applications, *J. Mater. Chem. C*, 2025, **13**, 3062.

17 W. Liu, L. Yuan, H. Wu, H. Dong and Y. Jin, Achieving broadband near-infrared emission with superior anti-thermal quenching by optimizing the excited-state population of Cr^{3+} in $Gd_3ScGa_4O_{12}$ garnet phosphors, *Mater. Horiz.*, 2024, **11**, 6399–6407.

18 C. Yang, X. Zou, M. Lyu, M. Wei, Z. Wang, X. Shuang, X. Zhang, B. Dong, X. Li, Y. Cong, M. Zheng, M. S. Molokeev and B. Lei, Towards promoting plant growth and fruit maturation: a highly efficient and thermally stable Cr^{3+} doped far-red phosphor, *J. Mater. Chem. C*, 2024, **12**, 12451–12457.

19 M. T. Tran, D. Q. Trung, N. Tu, D. D. Anh, L. T. H. Thu, N. V. Du, N. V. Quang, N. T. Huyen, N. D. T. Kien, D. X. Viet, N. D. Hung and P. T. Huy, Single-phase far-red-emitting $ZnAl_2O_4:Cr^{3+}$ phosphor for application in plant growth LEDs, *J. Alloys Compd.*, 2021, **884**, 161077.

20 X. Zhang, L. Dong, L. Zhang, Y. Xu, X. Wu, S. Yin, C. Zhong and H. You, High thermal stability phosphors with a rigid structure similar to the benzene ring and application in plant growth, *J. Mater. Chem. C*, 2022, **10**, 16857–16864.

 This journal is © the Partner Organisations 2025

Published on 21 Ciggilta Kudo 2025. Downloaded by Fail Open on 23/07/2025 10:35:15 AM.

21 H. Zeng, T. Zhou, L. Wang and R.-J. Xie, Two-Site Occupation for Exploring Ultra-Broadband Near-Infrared Phosphor—Double-Perovskite $La_2MgZrO_6:Cr^{3+}$, *Chem. Mater.*, 2019, **31**, 5245–5253.

22 L. Jiang, D. Yang, L. Zhang, J. Wang, J. Zhang, W. Jiang, G. Li, H. Yu, W. Si, Z. Shi, Z. Zhang and Y. Su, Concentration-dependent NIR emission of Cr^{3+} in a two-site occupancy within $K_4Ga_3Ta(PO_4)_6$, *J. Alloys Compd.*, 2025, **1010**, 177826.

23 V. Rajendran, M.-H. Fang, G. N. D. Guzman, T. Lesniewski, S. Mahlik, M. Grinberg, G. Leniec, S. M. Kaczmarek, Y.-S. Lin, K.-M. Lu, C.-M. Lin, H. Chang, S.-F. Hu and R.-S. Liu, Super Broadband Near-Infrared Phosphors with High Radiant Flux as Future Light Sources for Spectroscopy Applications, *ACS Energy Lett.*, 2018, **3**, 2679–2684.

24 Y. Tang, P. Lyu, D. Yin, Z. Liu, N. Pan, K. Li, Y. Ye, C. Xu and L. Sun, Ultra-broadband emission from $Mg_7Ga_2GeO_{12}:Ni^{2+}$, Cr^{3+} phosphor spanning the NIR I–III regions for spectroscopy applications, *Mater. Today Chem.*, 2024, **42**, 102364.

25 B.-M. Liu, X.-X. Guo, L.-Y. Cao, L. Huang, R. Zou, Z. Zhou and J. Wang, A High-efficiency blue-LED-excitable NIR-II-emitting $MgO:Cr^{3+},Ni^{2+}$ phosphor for future broadband light source toward multifunctional NIR spectroscopy applications, *Chem. Eng. J.*, 2023, **452**, 139313.

26 H. Suo, Y. Wang, X. Zhao, X. Zhang, L. Li, K. Guan, W. Ding, P. Li, Z. Wang and F. Wang, Rapid Nondestructive Detection Enabled by an Ultra–Broadband NIR pc–LED, *Laser Photonics Rev.*, 2022, **16**, 2200012.

27 C. Gong, S. Yang, Q. Zhang, J. He and X. Wang, Blue light excitable efficient down-conversion photoluminescence of Yb^{3+} and Er^{3+} in ultra-wide NIR region via Cr^{3+}-Yb^{3+}-Er^{3+} energy transfer in $KAlP_2O_7$ and multifunctional applications, *J. Alloys Compd.*, 2025, **1010**, 177842.

28 X. Zhang, D. Sun, P. Luo, L. Zhou, Z. Lu, J. Liu, C. Fan, X. Ye and H. You, Tunable luminescence via Cr^{3+}–Yb^{3+}/Nd^{3+} energy transfer in Cr^{3+} and Yb^{3+}/Nd^{3+} coactivated NIR phosphors for non-destructive analysis, *Inorg. Chem. Front.*, 2024, **11**, 8679–8689.

29 T. Zeng, P. Liu, G. Zeng, X. Yu, H. Liu, X. Zhu, W. Huang, G. Wang, L. Hou, M. Zhu, Y. Fang and T. Wang, Crystal Field-Engineered Cr^{3+}-Doped $Gd_3(Mg_xGa_{5-2x}Ge_x)O_{12}$ Phosphors for Near-Infrared LEDs and X-ray Imaging Applications, *Inorg. Chem.*, 2024, **63**, 12886–12893.

30 C. Wang, X. Zhang, C. Zhong, X. Wu, Y. Xu, S. Yin, Q. Yang, L. Zhou and H. You, Enhanced quantum efficiency and thermal stability by crystal-field engineering in a $Y(Ga,Al)_3(BO_3)_4:Cr^{3+},Yb^{3+}$ phosphor for diverse short-wave infrared applications, *J. Mater. Chem. C*, 2024, **12**, 3515–3525.

31 Y. Wang, Z. Wang, G. Wei, Y. Yang, S. He, J. Li, Y. Shi, R. Li, J. Zhang and P. Li, Highly Efficient and Stable Near–Infrared Broadband Garnet Phosphor for Multifunctional Phosphor–Converted Light–Emitting Diodes, *Adv. Opt. Mater.*, 2022, **10**, 2200415.

32 H. Cai, H. Chen, H. Zhou, J. Zhao, Z. Song and Q. L. Liu, Controlling Cr^{3+}/Cr^{4+} concentration in single-phase host toward tailored super-broad near-infrared luminescence for multifunctional applications, *Mater. Today Chem.*, 2021, **22**, 100555.

33 W. Yan, Y. Wei, M. S. Molokeev, S. Wang and G. Li, Green-emitting Bi^{3+}-doped $La_2SrSc_2O_7$ phosphor for pc-WLED lighting: Luminescent properties and energy transfer strategy, *J. Alloys Compd.*, 2022, **908**, 164621.

34 Z. Lu, D. Sun, S. Shen, Z. Lyu, L. Zhou, P. Luo, S. Wei and H. You, Efficient Energy Transfer for Near-Perfect Quantum Efficiency and Thermal Stability, *ACS Appl. Mater. Interfaces*, 2024, **16**, 31304–31312.

35 G. Liu and Z. Xia, Modulation of Thermally Stable Photoluminescence in Cr^{3+}-Based Near-Infrared Phosphors, *J. Phys. Chem. Lett.*, 2022, **13**, 5001–5008.